Published in final edited form as:
Phys Med Biol. 2014 August 21; 59(16): 4493–4504. doi:10.1088/0031-9155/59/16/4493.

Quantification of iopamidol multi-site chemical exchange properties for ratiometric chemical exchange saturation transfer (CEST) imaging of pH

Phillip Zhe Sun[1,*], **Dario Livio Longo**[2], **Wei Hu**[3], **Gang Xiao**[3,4], and **Renhua Wu**[3,*]

[1]Athinoula A. Martinos Center for Biomedical Imaging, Department of Radiology, Massachusetts General Hospital and Harvard Medical School, Charlestown, MA, USA

[2]Institute for Biostructures and Bioimages (CNR) c/o Molecular Biotechnology Center and Molecular Imaging Center, University of Torino, Italy

[3]Department of Radiology, 2nd Affiliated Hospital of Shantou University Medical College, China

[4]Department of Math and Applied Mathematics, Hanshan Normal University, Chaozhou, China

Abstract

pH-sensitive chemical exchange saturation transfer (CEST) MRI holds great promise for in vivo applications. However, CEST effect depends on not only exchange rate and hence pH, but also on the contrast agent concentration, which must be determined independently for pH quantification. Ratiometric CEST MRI normalizes the concentration effect by comparing CEST measurements of multiple labile protons to simplify pH determination. Iopamidol, a commonly used X-Ray contrast agent, has been explored as a ratiometric CEST agent for imaging pH. However, iopamidol CEST properties have not been solved, determination of which is important for optimization and quantification of iopamidol pH imaging. Our study numerically solved iopamidol multi-site pH-dependent chemical exchange properties. We found that iopamidol CEST MRI is suitable for measuring pH between 6 and 7.5 despite that T_1 and T_2 measurements varied substantially with pH and concentration. The pH MRI precision decreased with pH and concentration. The standard deviation of pH determined from MRI was 0.2 and 0.4 pH unit for 40 and 20 mM iopamidol solution of pH 6, and it improved to be less than 0.1 unit for pH above 7. Moreover, we determined base-catalyzed chemical exchange for 2-hydrooxypropanamido ($k_{sw}=1.2*10^{pH-4.1}$) and amide ($k_{sw}=1.2*10^{pH-4.6}$) protons that are statistically different from each other (P<0.01, ANCOVA), understanding of which should help guide in vivo translation of iopamidol pH imaging.

Keywords

chemical exchange saturation transfer (CEST); iopamidol; MRI; pH

*Corresponding author: Dr. Phillip Zhe Sun (pzhesun@nmr.mgh.harvard.edu), Athinoula A. Martinos Center for Biomedical Imaging, Department of Radiology, MGH and Harvard Medical School, Rm 2301, 149 13th Street, Charlestown, MA 02129, Phone: 617-726-4060, Fax: 617-726-7422, Or Dr. Renhua Wu (rhwu@stu.edu.cn), 2nd Affiliated Hospital of Shantou University Medical College, Shantou 515041, Guangdong, China, Tel: (86) 0754-88915674.

1. INTRODUCTION

Chemical exchange saturation transfer (CEST) MRI is sensitive to microenvironment properties including pH, temperature, metabolites, metal ions, and enzyme activities, and has been increasingly applied in vivo (Ward *et al.*, 2000; Aime *et al.*, 2002; Zhang *et al.*, 2005; Sun and Sorensen, 2008; Woods *et al.*, 2006; van Zijl and Yadav, 2011; Olatunde *et al.*, 2012; Dula *et al.*, 2012; Hingorani *et al.*, 2013; Vinogradov *et al.*, 2013; Castelli *et al.*, 2013). Particularly, CEST MRI is sensitive to pH, an informative biomarker for metabolic disruption in disorders such as acute ischemic stroke and renal injury (Jokivarsi *et al.*, 2007; Sun *et al.*, 2007b; Sun *et al.*, 2011a; Chan *et al.*, 2013; Jin *et al.*, 2012; Sun *et al.*, 2012). However, CEST MRI contrast varies not only with exchange rate, and hence pH, but also with the CEST agent concentration, bulk water relaxation rates and experimental conditions (Sun *et al.*, 2005; Terreno *et al.*, 2010; Wu *et al.*, 2012; Sun, 2012; Zaiss and Bachert, 2013; Sun *et al.*, 2014a). Because the labile proton concentration has to be independently determined in order to derive pH, the conventional CEST imaging only provides pH-weighted information (Sun, 2010b; Zu *et al.*, 2012; Sun *et al.*, 2013b). To address this limitation, ratiometric CEST MRI has been proposed that normalizes the confounding concentration effect for simplifying pH measurement (Ward and Balaban, 2000; Ali *et al.*, 2009; Liu *et al.*, 2012). A particularly interesting ratiometric MRI agent is iopamidol, approved by food and drug administration (FDA) as a X-Ray contrast agent since 1980s, which has been recently shown capable of imaging renal pH (Longo *et al.*, 2012; Longo *et al.*, 2011; Aime *et al.*, 2005).

Because of the tremendous interest in investigating iodinated agents for pH imaging, it is important to quantify their CEST properties, which should shed light on their sensitivity and detectability. Briefly, we used the Bloch–McConnell equations to describe multi-site iopamidol CEST effects (Woessner *et al.*, 2005; McMahon *et al.*, 2006; Sun *et al.*, 2007a; Li *et al.*, 2008; Murase and Tanki, 2011; Sun, 2010a). We numerically derived multi-site labile proton ratio and exchange rate, and found that chemical exchange for both 2-hydrooxypropanamido and amide protons are dominantly base-catalyzed for the range of pH we investigated. We also determined the accuracy of iopamidol pH imaging is 0.1 pH unit despite that T_1 and T_2 measurements varied substantially with pH and concentration. Because understanding of iopamidol exchange properties is necessary for optimizing the pulsed-RF irradiation in clinic, our study should aid clinical translation of iopamidol pH imaging (Sun *et al.*, 2008; Sun *et al.*, 2011b; Schmitt *et al.*, 2011; Sun *et al.*, 2013a; Zhu *et al.*, 2010; Zu *et al.*, 2011).

2. MATERIALS AND METHODS

Phantom

We prepared 20 and 40 mM iopamidol (Bracco Imaging, S.p.A., Milan, Italy) phosphate buffered solution with their pH titrated to 5.5, 6, 6.5, 7, 7.5 and 8 (EuTech pH Meter, Singapore). The solution was transferred into micro-centrifuge tubes and then inserted into two separate phantom containers. The phantom containers were filled with low gelling point agarose solution and solidified under room temperature.

MRI and Data Processing

Experiments were obtained using a 4.7 Tesla MRI scanner (Bruker Biospec, Billerica, MA) at room temperature. Image readout was single-shot echo planner imaging (EPI) with a field of view of 48×48 mm, image matrix =64×64 and slice thickness =3 mm. T_1 was measured using inversion recovery MRI, with seven inversion times (TI) ranging from 100 to 7,500 ms. We chose a long recovery time between image readout and the next inversion pulse to be 12,000 ms so that steady state could be obtained. The echo time (TE) was 39.5 ms and number of average (NSA) was 2. For T_2 MRI, we used SE EPI with six TE from 50 to 1,000 ms (TR=12,000 ms, NSA =2). For CEST MRI, we obtained Z-spectra ranging from −7 to 7 ppm, at intervals of 0.25 ppm (i.e., ±1400 Hz per 50 Hz at 4.7T). Continuous wave (CW) RF saturation was applied for 5 s (TS), with its amplitude varied from 1, 1.5, 2, 2.5, 3 to 4 μT (TR/TE =12,000/39.5 ms, NSA =2).

Data were processed in MATLAB (MathWorks, Natick, MA). T_1 and T_2 were obtained by least squares fitting of the image intensity as a function of inversion time and echo time, respectively. We fit asymmetry plots using modified Bloch–McConnell equations (Sun, 2010a). CEST effect was calculated using CEST ratio (CESTR)

$$\mathrm{CESTR}=\frac{\mathrm{I_{ref}}-\mathrm{I_{lebel}}}{\mathrm{I_0}} \quad (1)$$

where I_{ref} and I_{label} are the reference and label scans, and I_0 is the control scan (i.e., $B_1 = 0$). pH sensitive ratiometric CEST effect was calculated using relative CESTR and inverse relative saturation transfer (RST_{inv}), as defined by Longo et al (Longo *et al.*, 2011). Specifically, we have

$$\mathrm{rCESTR}=\mathrm{CESTR_{4.3ppm}}/\mathrm{CESTR_{5.5ppm}} \quad (2)$$

$$\begin{aligned}\mathrm{RST_{inv}}&=\frac{\mathrm{CESTR_{4.3ppm}}}{\mathrm{CESTR_{5.5ppm}}}\cdot\left(\frac{1-\mathrm{CESTR_{5.5ppm}}}{1-\mathrm{CESTR_{4.3ppm}}}\right)\\&=\mathrm{rCESTR}\cdot(1+\eta)\end{aligned} \quad (3)$$

where $\eta=\frac{\mathrm{CESTR_{4.3ppm}}-\mathrm{CESTR_{5.5ppm}}}{1-\mathrm{CESTR_{4.3ppm}}}$. In addition, the contrast to noise ratio (CNR) between pH 6 and 7.5 was calculated using (Sun *et al.*, 2013a)

$$\mathrm{CNR}=\frac{\mathrm{CESTR}|_{\mathrm{pH}=7.5}-\mathrm{CESTR}|_{\mathrm{pH}=6}}{\sqrt{\left(\sigma^2_{\mathrm{pH}=7.5}+\sigma^2_{\mathrm{pH}=6}\right)/2}} \quad (4)$$

where CESTR and σ represent the mean CESTR and its standard deviation for each pH compartment. For the numerical fitting, we fixed the relative labile proton ratio for 5.5 (2-hydrooxypropanamido group), 4.3 (amide group), 1.8 (secondary hydroxyl group) and 0.8 (primary hydroxyl groups) ppm be 1:2:1:4. Eleven parameters were determined from the numerical fitting, including T_{1w}, T_{2w}, 2-hydrooxypropanamido labile proton ratio, and labile proton exchange rate and T_{2s} for each labile proton at 5.5, 4.3, 1.8 and 0.8 ppm. We used least squares optimization to minimize the error function, given as

NIH-PA Author Manuscript
NIH-PA Author Manuscript

$\varepsilon = \sum_{\delta=0.75}^{7\text{ppm}} \left(\text{CSETR}_{\text{fit}}(\delta) - \text{CSETR}_{\text{exp}}(\delta)\right)^2$. The fitting was repeated for each pH and RF power level. Results were reported as mean ± standard deviation and P values less than 0.05 were considered statistically significant.

3. RESULTS

Fig. 1 compares simulated Z-spectra and asymmetry plots of two exchangeable sites at 4.3 and 5.5 ppm with their labile proton ratio with respect to bulk water being 1:1500 and 1:3000 at exchange rates of 50 and 200 s^{-1}, respectively (B_1 =2.5 μT, TS =5 s). We chose representative relaxation rates of T_{1w} =3 s, T_{1s} =1 s, T_{2s} =0.5 s, and varied T_{2w} from 1 to 2 s. CEST effects could be observed at 4.3 and 5.5 ppm (Fig. 1a). Z-spectral signal close to the bulk water resonance strongly depends on T_{2w} due to direct RF saturation. Because the asymmetry analysis subtracts the symmetric direct RF saturation effect, it is substantially less susceptible to T_{2w} variation. We measured the change in Z-spectra and asymmetry plots from those simulated assuming the median T_{2w} (i.e., 1.5 s). Fig. 1b shows that the normalized sum of squares (i.e., $\sum_{i=1}^{N} \left(I_{i,T_{2w}} - I_{i,\overline{T_{2w}}}\right)^2 / N$) is significantly higher in Z-spectrum than asymmetry plot (2.85±3.06 vs. 0.01 ±0.01, P<0.01). Because the asymmetry plot is less susceptible to moderate T_{2w} difference than Z-spectra, we chose to solve iopamidol CEST properties by fitting the asymmetry plots.

Fig. 2 evaluates pH-sensitive iopamidol CEST imaging. Fig. 2a shows three representative Z-spectra at pH of 6, 7 and 8 (B_1 =2.5 μT). It is important to note that CEST effects from amide (4.3 ppm) and 2-hydrooxypropanamido (5.5 ppm) could be reasonably resolved for pH 6 and 7, they however, merged into one broad peak at pH of 8. Fig. 2b shows CEST asymmetry ratio (CESTR) calculated at 4.3 (circles) and 5.5 ppm (squares). While CEST effect initially increased with pH, CESTR at 5.5 ppm peaked at pH of 7 and CESTR at 4.3 ppm peaked at pH of 7.5 (Fig. 2b). The unequal pH dependence of CESTR at 4.3 and 5.5 ppm enables ratiometric pH quantification. Fig. 2c shows that the rCESTR increases from 0.6 ± 0.1 to 2.3 ± 0.1 for pH at 6 and 7.5, respectively. We also measured T_1 and T_2. T_1 decreased substantially with concentration (P<0.01, 2-sample t-test) but showed little pH dependence (P>0.15, linear regression). T_{1w} was 2.68 ± 0.01s and 2.51 ± 0.01 s for 20 and 40 mM iopamidol solutions, respectively. In contrast, T_2 decreased substantially with pH (P<0.01, linear regression) and concentration (P<0.01, paired t-test). For 20 mM iopamidol solution, T_{2w} (pH)=2.46−0.23*pH (s), whereas for 40 mM, T_{2w} (pH)=1.93−0.20*pH (s).

We investigated the optimal RF irradiation level for ratiometric pH imaging. Fig. 3 a shows measured CESTR at 4.3 (circles) and 5.5 ppm (squares) for pH of 6 and 7.5 (B_1=2.5 μT). CESTR increased with RF irradiation level, suggesting that a relatively high B_1 irradiation field is needed to efficiently saturate iopamidol labile groups. Whereas CESTR at 5.5 ppm was higher than that at 4.3 ppm for pH of 6, the relative magnitude of CEST effect at 5.5 and 4.3 ppm reversed at pH of 7.5. We quantified ratiometric pH MRI using two indices: rCESTR and $RST_{inv,}$ as defined by Longo et al (Longo *et al.*, 2011). The contrast to noise ratio (CNR) between pH 6 and 7.5 compartments initially increased with B_1 and peaked at an intermediate B_1 of 2.5 μT (Fig. 3b). This shows that whereas the magnitude of pH contrast measured by ΔRST_{inv} is statistically higher than that of ΔrCESTR (P<0.01, ANCOVA), there was relatively small difference in CNR up to the optimal B_1 saturation field. Fig. 3c shows the ratiometric CESTR map, demonstrating good pH contrast between 6 and 7.5.

We determined the accuracy of iopamidol pH mapping. Fig. 4a shows that the logarithmic rCESTR can be described by polynomial regression ($\log_{10}(rCESTR)=0.13*pH^2-1.34*pH+3.26$) for 40 mM iopamidol solution, with $R^2=0.998$ (P<0.01). The polynomial regression enables derivation of absolute pH map from pH-weighted rCESTR image for 40 mM (Fig. 4b) and 20 mM iopamidol (Fig. 4c). For 40 mM iopamidol, we found pH being 5.99±0.23, 6.46±0.06, 7.03±0.02 and 7.49±0.02 for pH of 6.0, 6.5, 7.0 and 7.5, respectively. pH determined from MRI strongly correlates with calibrated pH, pH(MRI)=1.01*pH−0.10 (P<0.01). Moreover, the intercept is not significant different from zero, suggesting no systematic biases in pH determination. For 20 mM iopamidol, we found pH being 6.01±0.36, 6.46±0.20, 7.09±0.08 and 7.55±0.08 for pH of 6.0, 6.5, 7.0 and 7.5, respectively. We found pixel-wise determined pH for 20 mM iopamidol is pH(MRI)=1.03*pH-0.15 (P<0.01). The intercept is not statistically significant different from zero (Fig. 4d). Our data showed that the standard deviation was higher at lower pH and iopamidol concentration, suggesting that it is governed by signal to noise ratio (SNR) of CEST MRI measurement. This is because exchange rate is reduced at lower pH, hence the CEST effect and SNR decrease with pH and iopamidol concentration. The pH MRI precision decreased with pH and concentration. The standard deviation of pH determined from MRI was 0.2 and 0.4 pH unit for 40 and 20 mM iopamidol solution of pH 6, and it improved to be less than 0.1 unit for pH above 7, for a voxel size of 1.69 mm^3. This was because the signal noise to ratio (SNR) of CEST imaging decreases with CEST effect, hence, iopamidol concentration and pH (Sun *et al.*, 2013a). Because SNR can be improved with signal averaging, use of sensitive hardware and novel pulse sequence, the precision of pH MRI could be further improved (Sun *et al.*, 2014b). Both χ^2 and R^2 tests showed good fitting. We found χ^2 was less than 10^{-3} for pH measurement from both iopamidol solutions, substantially smaller than $\chi^2_{0.05}$ (i.e., 7.82) for three degrees of freedom. In addition, R^2 was higher than 0.99 for pH measurement from both iopamidol solutions. Furthermore, ANCOVA analysis of pH measurements from 20 and 40 mM iopamidol phantoms showed no significant effect of iopamidol concentration on pH calibration, confirming that iopamidol ratiometric pH imaging can indeed measure pH despite a substantial difference in iopamidol concentration. Nevertheless, these are preliminary findings that need to be further improved in terms of precision in order to be clinically applicable.

We numerically solved iopamidol CEST properties using the Bloch-McConnell equations. Because CEST peaks could not be resolved at pH of 8 due to very fast chemical exchange, we numerically fit CEST asymmetry plots for pH from 5.5 to 7.5 under B_1 irradiation level of 1, 1.5, 2, 2.5, 3 and 4 μT. Due to non-negligible CEST effects from hydroxyl groups, a five-pool exchange model was chosen to describe iopamidol CEST measurements, including 2-hydrooxypropanamido protons (5.5 ppm), amide (4.3 ppm), two chemically not-equivalent hydroxyl groups (1.8 and 0.8 ppm) and bulk water (set to be 0 ppm). In addition, we set

NIH-PA Author Manuscript

NIH-PA Author Manuscript

labile proton T_1 (T_{1s}) to be 1 s due to the use of long RF irradiation. B_0 inhomogeneity was determined to be 5±6 Hz. Nevertheless, to reduce field inhomogeneity effect very close to bulk water signal, we fit CEST asymmetry from 0.75 to 7 ppm. The numerical fitting and experimental data under the optimal RF power level of 2.5 μT were shown in Fig. 5a. The coefficient of determination (R^2) for all pH values was 0.99 ±0.01, and the squared residuals between numerical fitting and experimental measurements was 0.30±0.77%. The fitting took approximately 4 min for each RF power level. Fig. 5b shows that the exchange rate at 4.3 and 5.5 ppm can be reasonably described using a dominantly base-catalyzed exchange equation (i.e., $k_{sw}=k_0+k_b\cdot 10^{pH-pkw}$). We found k_{sw}(5.5 ppm)=$1.2\cdot 10^{pH-4.1}$ for 2-hydrooxypropanamido protons and k_{sw}(4.3 ppm)=$1.2\cdot 10^{pH-4.6}$ for amide protons (Table 1). Statistical test of logarithmic exchange rate confirmed significant difference in their exchange rate (P<0.01, ANCOVA). In addition, the 2-hydrooxypropanamido labile proton ratio with respect to bulk water can be estimated to be 1:2778, while that solved from numerical fitting was 1:3449 ± 747, not significantly different from the theoretical estimation (P>0.05, one sample t-test). Moreover, numerical fitting determined T_{1w}=3.5±0.3 s, T_{2w}=1.6±0.1 s, and T_{2s} was 0.6±0.3, 1.5±0.4, 0.7±0.4 and 0.8±0.2 s for 2-hydrooxypropanamido protons (5.5 ppm), amide (4.3 ppm), and two hydroxyl groups at (1.8 and 0.8 ppm), respectively. Understanding pH-dependent exchange properties should help guide experimental optimization and quantification of iopamidol pH imaging under various experimental conditions such as pulsed RF irradiation scheme at different field strength.

4. DISCUSSION

Our study quantitatively solved the multi-site exchange properties of iopamidol. We confirmed that iopamidol ratiometric CEST MRI is capable of measuring pH from 6 to 7.5 at 4.7 T with an accuracy of 0.1 pH unit despite that T_1 and T_2 measurements varied substantially with pH and concentration. Iopamidol pH imaging is promising to complement pH measurement techniques including pH-weighted CEST MRI, ^{31}P MR spectroscopy (MRS), and dual modality (positron emission tomography (PET)-MRI) contrast-enhanced imaging (Adam *et al.*, 1986; Frullano *et al.*,; Sheth *et al.*, 2012). Clinical iopamidol dosage is procedure specific. For example, the recommended dosage is 40–150 ml of Isovue 300–370 for whole body computer tomography enhancement (Iopamidol Product Monograph). In this case, the iopamidol concentration in blood can be estimated to be about 6–29 mM. Iopamidol concentration is also organ specific, likely being more concentrated in kidney and bladder. Indeed, Longo et al. have successfully imaged acute renal injury-induced pH change using iopamidol ratiometric CEST MRI (Longo *et al.*, 2012). Accurate pH imaging can complement a number of MRI applications (Kogan *et al.*, 2014; Dagher *et al.*, 2000). For example, Dagher et al. showed that urea, an important kidney metabolite, can be imaged using CEST MRI (Dagher *et al.*, 2000). Because urea hydroxyl chemical exchange is pH-dependent, pH has to be measured independently in order to derive urea concentration, for which iopamidol pH MRI is applicable.

Because high magnetic field provides enhanced sensitivity for diamagnetic CEST (DIACEST) MRI, iodinated contrast agent-based pH imaging has been initially demonstrated at 7 Tesla (Chen *et al.*, 2013; Longo *et al.*, 2012). In addition to more efficient spin polarization, T_1 also increases at high field strength, leading to stronger CEST effect.

NIH-PA Author Manuscript

NIH-PA Author Manuscript

Moreover, because the frequency shift in Hz scales linearly with field strength, the concomitant direct RF saturation is reduced at high field. We here demonstrated iopamidol pH imaging at 4.7 Tesla, substantiating its translation potential. We also compared two means of pH calculation: rCESTR and RST_{inv}. Whereas ΔRST_{inv} is statistically larger than ΔrCESTR between pH 6 and 7.5, there was relatively small difference in their CNR due to error propagation from the correction factor (Fig. 3). It is important to note that because our ability to resolve pH difference relies upon CNR, both rCESTR and RST_{inv} provide similar pH sensitivity. Our study showed that pH can be accurately determined despite substantial pH and iopamidol concentration-induced T_1 and T_2 change. Also, worth noting is that iopamidol labile proton groups are reasonably close to endogenous amide protons and semisolid macromolecules, which may have to be considered in order to quantify in vivo ratiometric pH imaging (Henkelman *et al.*, 1994; Zhou *et al.*, 2004; Jones *et al.*, 2013; Scheidegger *et al.*, 2011). It has been shown by Chen et al. that Lorentzian line shape fitting could overcome the NOE and MT contributions and enable extracellular pH determination within in vivo tumors (Chen *et al.*, 2013).

It is necessary to note that it is technically challenging to determine exchange properties in a multi-site CEST system. T_2-based solution could not resolve multi-site exchange (Aime *et al.*, 2005). Although the Lorentzian spectral analysis is capable of estimating exchange rate, it is difficult to solve multi-site exchange that are close to each other (Allerhand *et al.*, 1966). Our work addressed an important aspect of quantitative CEST analysis. We showed that the modified Bloch-McConnell equations can reasonably describe multi-site CEST phenomenon, with small residual errors between the fitting and experimental measurement. The numerically solved labile proton ratio is in reasonable agreement with estimation, and the exchange rate can be well described by a base-catalyzed chemical exchange relationship. While it is necessary to include hydroxyl groups in order to fit the asymmetry plots at 4.3 and 5.5 ppm, hydroxyl chemical exchange rates are in the fast exchange regime. Therefore, the numerically derived exchange rates for hydroxyl groups may be subject to non-negligible fitting errors but provide good estimates of their order of magnitude. It is important to note that understanding pH-dependent exchange properties could help guide experimental optimization and quantification of iopamidol pH imaging. Briefly, because continuous wave (CW) RF irradiation scheme is not routinely available on clinical scanners, pulsed RF irradiation has to be chosen. The irradiation pulse duration, flip angle and inter-pulse delay of CEST MRI have to be optimized based on chemical exchange rate and pulse sequence (Sun *et al.*, 2008; Sun *et al.*, 2011b; Schmitt *et al.*, 2011; Sun *et al.*, 2013a; Zhu *et al.*, 2010; Sun *et al.*, 2014b). Therefore, determination of pH-dependent exchange rate should aid clinical translation of iopamidol pH imaging.

5. CONCLUSION

Our study numerically derived multi-site iopamidol exchange properties and showed that chemical exchange rates for 2-hydrooxypropanamido and amide groups were dominantly base-catalyzed and statistically different from each other, making iopamidol a sensitive ratiometric pH MRI agent. We further showed that the sensitivity of iopamidol pH imaging peaked at an intermediate RF irradiation level, and iopamidol CEST MRI is suitable for measuring pH between 6 and 7.5 despite that T_1 and T_2 measurements varied substantially with pH and concentration. Our study remains promising to help optimize and translate iopamidol pH imaging to the clinic.

Acknowledgments

This study was supported in part by grants from NIH/NIBIB 1K01EB009771, NIH/NINDS 1R01NS083654, Regione Piemonte (NanoIGT-CIPE2007) and NSFC 30930027. The authors would like to thank Dr. Chongzhao Ran for helpful discussions and Bracco Imaging, S.p.A., Milan, Italy for generously providing iopamidol samples.

References

Adam WR, Koretsky AP, Weiner MW. 31P-NMR in vivo measurement of renal intracellular pH: effects of acidosis and K+ depletion in rats. Am J Physiol Cell Physiol. 1986; 251:F904–10.

Aime S, Barge A, Delli Castelli D, Fedeli F, Mortillaro A, Nielsen FU, Terreno E. Paramagnetic Lanthanide(III) complexes as pH-sensitive chemical exchange saturation transfer (CEST) contrast agents for MRI applications. Magn Reson Med. 2002; 47:639–48. [PubMed: 11948724]

Aime S, Calabi L, Biondi L, Miranda MD, Ghelli S, Paleari L, Rebaudengo C, Terreno E. Iopamidol: Exploring the potential use of a well-established x-ray contrast agent for MRI. Magn Reson Med. 2005; 53:830–4. [PubMed: 15799043]

Ali MM, Liu G, Shah T, Flask CA, Pagel MD. Using Two Chemical Exchange Saturation Transfer Magnetic Resonance Imaging Contrast Agents for Molecular Imaging Studies. Acc Chem Res. 2009; 42:915–24. [PubMed: 19514717]

Allerhand A, Gutowsky H, Jonas J, Meinzer R. Nuclear magnetic resonance methods for determining chemical-exchange rates. J Am Chem Soc. 1966; 88:3185–93. [PubMed: 5946590]

Castelli DD, Terreno E, Longo D, Aime S. Nanoparticle-based chemical exchange saturation transfer (CEST) agents. NMR in Biomedicine. 2013; 26:839–49. [PubMed: 23784956]

Chan KWY, Liu G, Song X, Kim H, Yu T, Arifin DR, Gilad AA, Hanes J, Walczak P, van Zijl PCM, Bulte JWM, McMahon MT. MRI-detectable pH nanosensors incorporated into hydrogels for in vivo sensing of transplanted-cell viability. Nat Mater. 2013; 12:268–75. [PubMed: 23353626]

Chen LQ, Howison CM, Jeffery JJ, Robey IF, Kuo PH, Pagel MD. Evaluations of extracellular pH within in vivo tumors using acidoCEST MRI. Magn Reson Med. 2013 in press.

Dagher AP, Aletras A, Choyke P, Balaban RS. Imaging of urea using chemical exchange-dependent saturation transfer at 1.5T. J Magn Reson Imaging. 2000; 12:745–8. [PubMed: 11050645]

Dula AN, Asche EM, Landman BA, Welch EB, Pawate S, Sriram S, Gore JC, Smith SA. Development of chemical exchange saturation transfer at 7T. Magn Reson Med. 2012; 66:831–8. [PubMed: 21432902]

Frullano L, Catana C, Benner T, Sherry AD, Caravan P. Bimodal MR–PET Agent for Quantitative pH Imaging. Angew Chem Int Ed Engl. 2010; 49:2382–4. [PubMed: 20191650]

Henkelman RM, Stanisz GJ, Kim JK, Bronskill MJ. Anisotropy of NMR properties of tissues. Magn Reson Med. 1994; 32:592–601. [PubMed: 7808260]

Hingorani DV, Randtke EA, Pagel MD. A CatalyCEST MRI Contrast Agent That Detects the Enzyme-Catalyzed Creation of a Covalent Bond. J Am Chem Soc. 2013; 135:6396–8. [PubMed: 23601132]

Jin T, Wang P, Zong X, Kim S-G. Magnetic resonance imaging of the Amine Proton EXchange (APEX) dependent contrast. NeuroImage. 2012; 16:1218–27. [PubMed: 21871570]

Jokivarsi KT, Gröhn HI, Gröhn OH, Kauppinen RA. Proton transfer ratio, lactate, and intracellular pH in acute cerebral ischemia. Magn Reson Med. 2007; 57:647–53. [PubMed: 17390356]

Jones CK, Huang A, Xu J, Edden RAE, SchÃ¤r M, Hua J, Oskolkov N, ZacÃ D, Zhou J, McMahon MT, Pillai JJ, van Zijl PCM. Nuclear Overhauser enhancement (NOE) imaging in the human brain at 7 T. NeuroImage. 2013; 77:114–24. [PubMed: 23567889]

Kogan F, Haris M, Singh A, Cai K, Debrosse C, Nanga RPR, Hariharan H, Reddy R. Method for highresolution imaging of creatine in vivo using chemical exchange saturation transfer. Magn Reson Med. 2014; 71:164–72. [PubMed: 23412909]

Li AX, Hudson RHE, Barrett JW, Johns CK, Pasternak SH, Bartha R. Four-pool modeling of proton exchange processes in biological systems in the presence of MRI-paramagnetic chemical exchange saturation transfer (PARACEST) agents. Magn Reson Med. 2008; 60:1197–206. [PubMed: 18958857]

Liu G, Li Y, Sheth VR, Pagel MD. Imaging In Vivo Extracellular pH with a Single Paramagnetic Chemical Exchange Saturation Transfer Magnetic Resonance Imaging Contrast Agent. Molecular Imaging. 2012; 11:47–57. [PubMed: 22418027]

Longo DL, Busato A, Lanzardo S, Antico F, Aime S. Imaging the pH evolution of an acute kidney injury model by means of iopamidol, a MRI-CEST pH-responsive contrast agent. Magn Reson Med. 2012; 70:859–64.

Longo DL, Dastrù W, Digilio G, Keupp J, Langereis S, Lanzardo S, Prestigio S, Steinbach O, Terreno E, Uggeri F, Aime S. Iopamidol as a responsive MRI-chemical exchange saturation transfer contrast agent for pH mapping of kidneys: In vivo studies in mice at 7 T. Magn Reson Med. 2011; 65:202–11. [PubMed: 20949634]

McMahon M, Gilad A, Zhou J, Sun PZ, Bulte J, van Zijl PC. Quantifying exchange rates in chemical exchange saturation transfer agents using the saturation time and saturation power dependencies of the magnetization transfer effect on the magnetic resonance imaging signal (QUEST and QUESP): Ph calibration for poly-L-lysine and a starburst dendrimer. Magn Reson Med. 2006; 55:836–47. [PubMed: 16506187]

Murase K, Tanki N. Numerical solutions to the time-dependent Bloch equations revisited. Magn Reson Imaging. 2011; 29:126–31. [PubMed: 20832224]

Olatunde AO, Dorazio SJ, Spernyak JA, Morrow JR. The NiCEST Approach: Nickel(II) ParaCEST MRI Contrast Agents. J Am Chem Soc. 2012; 134:18503–5. [PubMed: 23102112]

Scheidegger R, Vinogradov E, Alsop DC. Amide proton transfer imaging with improved robustness to magnetic field inhomogeneity and magnetization transfer asymmetry using saturation with frequency alternating RF irradiation. Magn Reson Med. 2011; 66:1275–85. [PubMed: 21608029]

Schmitt B, Zaiß M, Zhou J, Bachert P. Optimization of pulse train presaturation for CEST imaging in clinical scanners. Magn Reson Med. 2011; 65:1620–9. [PubMed: 21337418]

Sheth VR, Li Y, Chen LQ, Howison CM, Flask CA, Pagel MD. Measuring in vivo tumor pHe with CEST-FISP MRI. Magn Reson Med. 2012; 67:760–8. [PubMed: 22028287]

Sun PZ. Simplified and scalable numerical solution for describing multi-pool chemical exchange saturation transfer (CEST) MRI contrast. J Magn Reson. 2010a; 205:235–41. [PubMed: 20570196]

Sun PZ. Simultaneous determination of labile proton concentration and exchange rate utilizing optimal RF power: radio frequency power (RFP) dependence of chemical exchange saturation transfer (CEST) MRI. J Magn Reson. 2010b; 202:155–61. [PubMed: 19926319]

Sun PZ. Simplified quantification of labile proton concentration-weighted chemical exchange rate (kws) with RF saturation time dependent ratiometric analysis (QUESTRA): Normalization of relaxation and RF irradiation spillover effects for improved quantitative chemical exchange saturation transfer (CEST) MRI. Magn Reson Med. 2012; 67:936–42. [PubMed: 21842497]

Sun PZ, Benner T, Kumar A, Sorensen AG. Investigation of optimizing and translating pH-sensitive pulsed-chemical exchange saturation transfer (CEST) imaging to a 3T clinical scanner. Magn Reson Med. 2008; 60:834–41. [PubMed: 18816867]

Sun PZ, Cheung JS, Wang EF, Lo EH. Association between pH-weighted endogenous amide proton chemical exchange saturation transfer MRI and tissue lactic acidosis during acute ischemic stroke. J Cereb Blood Flow Metab. 2011a; 31:1743–50. [PubMed: 21386856]

Sun PZ, Lu J, Wu Y, Xiao G, Wu R. Evaluation of the dependence of CEST-EPI measurement on repetition time, RF irradiation duty cycle and imaging flip angle for enhanced pH sensitivity. Phys Med Biol. 2013a; 58:N229–N40. [PubMed: 23939228]

Sun PZ, Sorensen AG. Imaging pH using the chemical exchange saturation transfer (CEST) MRI: correction of concomitant RF irradiation effects to quantify CEST MRI for chemical exchange rate and pH. Magn Reson Med. 2008; 60:390–7. [PubMed: 18666128]

Sun PZ, van Zijl PCM, Zhou J. Optimization of the irradiation power in chemical exchange dependent saturation transfer experiments. J Magn Reson. 2005; 175:193–200. [PubMed: 15893487]

Sun PZ, Wang EF, Cheung JS. Imaging acute ischemic tissue acidosis with pH-sensitive endogenous amide proton transfer (APT) MRI – Correction of tissue relaxation and concomitant RF irradiation effects toward mapping quantitative cerebral tissue pH. Neuroimage. 2012; 60:1–6. [PubMed: 22178815]

Sun PZ, Wang EF, Cheung JS, Zhang XA, Benner T, Sorensen AG. Simulation and optimization of pulsed radio frequency (RF) irradiation scheme for chemical exchange saturation transfer (CEST) MRI – demonstration of pH-weighted pulsed-amide proton CEST MRI in an animal model of acute cerebral ischemia. Magn Reson Med. 2011b; 66:1042–8. [PubMed: 21437977]

Sun PZ, Wang Y, Dai Z, Xiao G, Wu R. Quantitative chemical exchange saturation transfer (qCEST) MRI – RF spillover effect-corrected omega plot for simultaneous determination of labile proton fraction ratio and exchange rate. Contrast Media Mol Imaging. 2014a; 9:268–75. [PubMed: 24706610]

Sun PZ, Wang Y, Lu J. Sensitivity-enhanced chemical exchange saturation transfer (CEST) MRI with least squares optimization of Carr Purcell Meiboom Gill multi-echo echo planar imaging. Contrast Media & Molecular Imaging. 2014b; 9:177–81. [PubMed: 24523063]

Sun PZ, Wang Y, Xiao G, Wu R. Simultaneous experimental determination of labile proton fraction ratio and exchange rate with irradiation radio frequency power-dependent quantitative CEST MRI analysis. Contrast Media Mol Imaging. 2013b; 8:246–51. [PubMed: 23606428]

Sun PZ, Zhou J, Huang J, van Zijl P. Simplified quantitative description of amide proton transfer (APT) imaging during acute ischemia. Magn Reson Med. 2007a; 57:405–10. [PubMed: 17260362]

Sun PZ, Zhou J, Sun W, Huang J, van Zijl PC. Detection of the ischemic penumbra using pH-weighted MRI. J Cereb Blood Flow Metab. 2007b; 27:1129–36. [PubMed: 17133226]

Terreno E, Dastrù W, Delli Castelli D, Gianolio E, Geninatti Crich S, Longo D, Aime S. Advances in metal-based probes for MR molecular imaging applications. Curr Med Chem. 2010; 17:3684–70. [PubMed: 20846110]

van Zijl PCM, Yadav N. Chemical exchange saturation transfer (CEST): What is in a name and what isn't? Magn Reson Med. 2011; 65:927–48. [PubMed: 21337419]

Vinogradov E, Sherry AD, Lenkinski RE. CEST: From basic principles to applications, challenges and opportunities. J Magn Reson. 2013; 229:155–72. [PubMed: 23273841]

Ward KM, Aletras AH, Balaban RS. A new class of contrast agents for MRI based on proton chemical exchange dependent saturation transfer (CEST). J Magn Reson. 2000; 143:79–87. [PubMed: 10698648]

Ward KM, Balaban RS. Determination of pH using water protons and chemical exchange dependent saturation transfer (CEST). Magnetic Resonance in Medicine. 2000; 44:799–802. [PubMed: 11064415]

Woessner DE, Zhang S, Merritt ME, Sherry AD. Numerical solution of the Bloch equations provides insights into the optimum design of PARACEST agents for MRI. Magn Reson Med. 2005; 53:790–9. [PubMed: 15799055]

Woods M, Woessner DE, Sherry AD. Paramagnetic lanthanide complexes as PARACEST agents for medical imaging. Chem Soc Rev. 2006; 35:500–11. [PubMed: 16729144]

Wu R, Liu C, Liu P, Sun PZ. Improved measurement of labile proton concentration-weighted chemical exchange rate (kws) with experimental factor-compensated and T1-normalized quantitative chemical exchange saturation transfer (CEST) MRI. Contrast Media Mol Imaging. 2012; 7:384–9. [PubMed: 22649044]

Zaiss M, Bachert P. Exchange-dependent relaxation in the rotating frame for slow and intermediate exchange – modeling off-resonant spin-lock and chemical exchange saturation transfer. NMR in Biomedicine. 2013; 26:507–18. [PubMed: 23281186]

Zhang S, Malloy CR, Sherry AD. MRI Thermometry Based on PARACEST Agents. J Am Chem Soc. 2005; 127:17572–3. [PubMed: 16351064]

Zhou J, Wilson DA, Sun PZ, Klaus JA, van Zijl PCM. Quantitative description of proton exchange processes between water and endogenous and exogenous agents for WEX, CEST, and APT experiments. Magn Reson Med. 2004; 51:945–52. [PubMed: 15122676]

Zhu H, Jones CK, van Zijl PCM, Barker PB, Zhou J. Fast 3D chemical exchange saturation transfer (CEST) imaging of the human brain. Magn Reson Med. 2010; 64:638–44. [PubMed: 20632402]

NIH-PA Author Manuscript

NIH-PA Author Manuscript

Zu Z, Janve VA, Li K, Does MD, Gore JC, Gochberg DF. Multi-angle ratiometric approach to measure chemical exchange in amide proton transfer imaging. Magn Reson Med. 2012; 68:711–9. [PubMed: 22161770]

Zu Z, Li K, Janve VA, Does MD, Gochberg DF. Optimizing pulsed-chemical exchange saturation transfer imaging sequences. Magn Reson Med. 2011; 66:1100–8. [PubMed: 21432903]

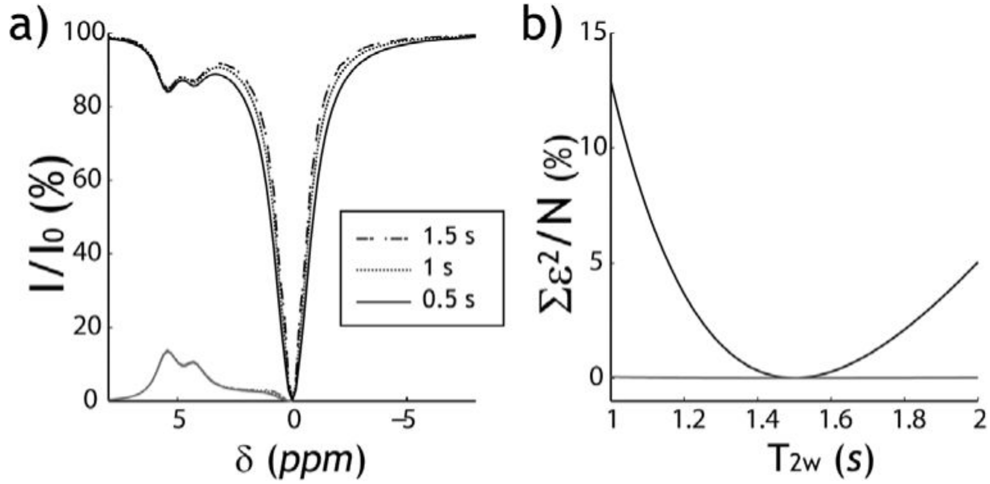

Fig. 1.

a) Simulated CEST Z-spectra and asymmetry-plots for three representative bulk water T_{2w} of 0.5, 1 and 1.5 s. (B_1 =2.5 μT). b) Two plots of sum of squares analysis of the difference in simulated CEST Z-spectra (black) and asymmetry plots (gray) as a function of T_2w from those obtained assuming the median T_{2w} (i.e., $\sum_{i=1}^{N}\left(I_{i,_{T_{2w}}} - I_{i,_{\overline{T_{2w}}}}\right)^2/N$).

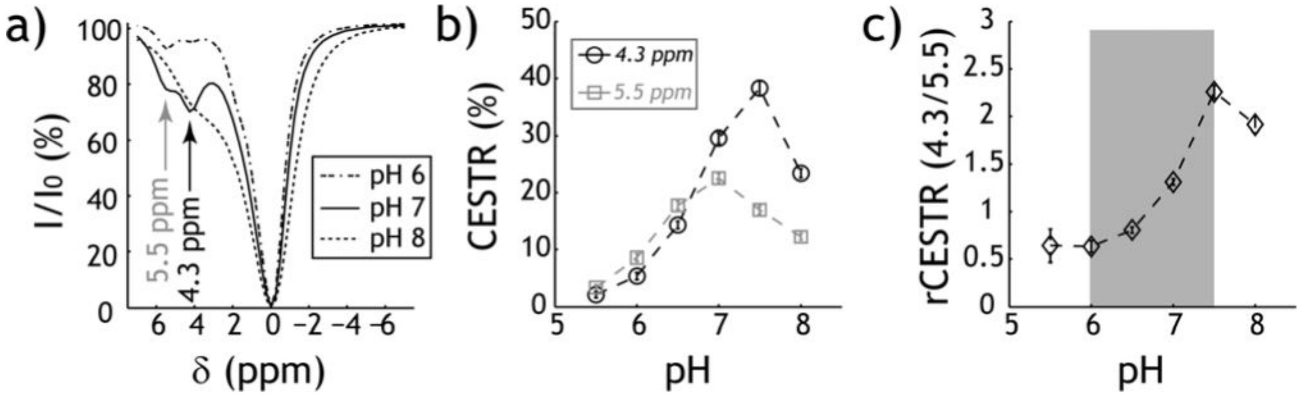

Fig. 2.

Iopamidol ratiometric pH MRI. a) Z-spectra for representative pH of 6, 7 and 8 (B_1 =2.5 μT, TS =5s) at room temperature. b) CEST ratio (CESTR) calculated from the asymmetry analysis as a function of pH. CESTR at 4.3 ppm peaks at pH 7.5 while CESTR of 5.5 ppm peaks at pH 7. c) Ratiometric CEST analysis is sensitive to pH ranging from 6 to 7.5.

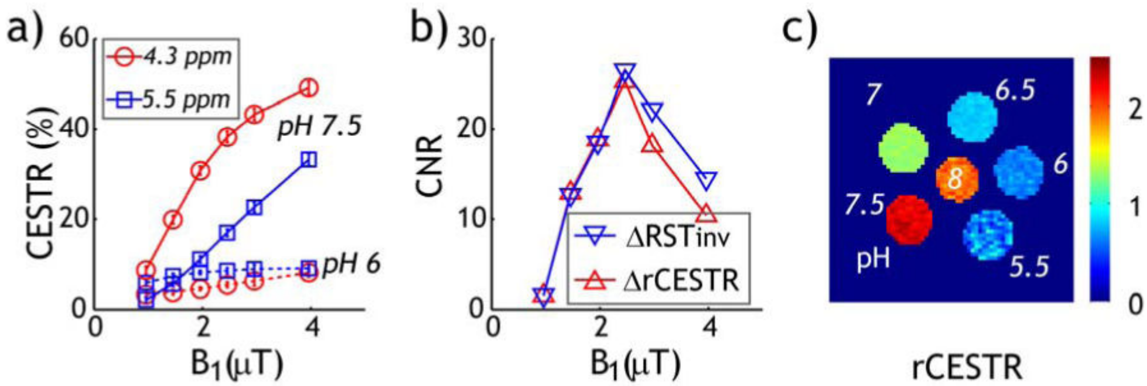

Fig. 3.

B_1-dependence of iopamidol ratiometric pH MRI. a) CESTR at 4.3 and 5.5 ppm increases with B_1 irradiation level for representative pH of 6 and 7.5. b) CNR in ratiometric pH MRI between pH of 6 and 7.5 peaks under an intermediate optimal B_1 level of 2.5 μT. c) pH-weighted rCESTR map (B_1 =2.5 μT).

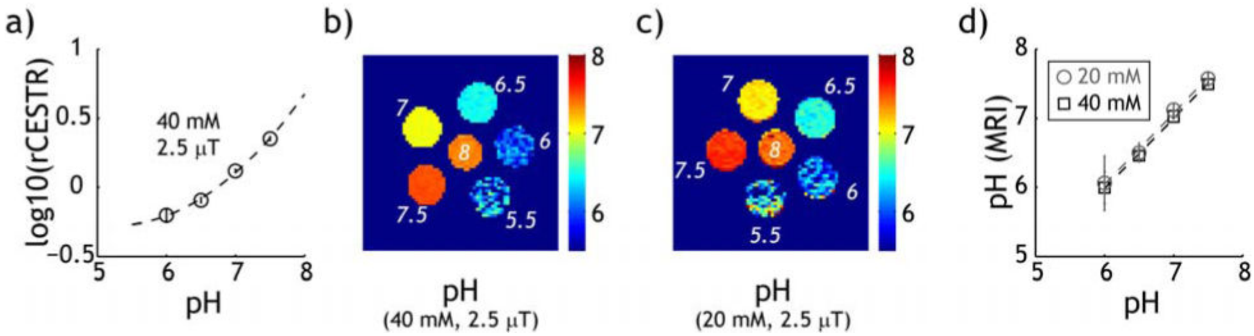

Fig. 4.

Evaluation of the accuracy of iopamidol pH imaging. a) Logarithmic rCESTR as a function of pH for 40 mM iopamidol. b) pH map determined from pH-weighted rCESTR map for 40 mM iopamidol. c) pH map determined from pH-weighted rCESTR map for 20 mM iopamidol. d) pH determined from iopamidol pH MRI vs. titrated pH for 20 mM (circles) and 40 mM (squares) iopamidol phantoms.

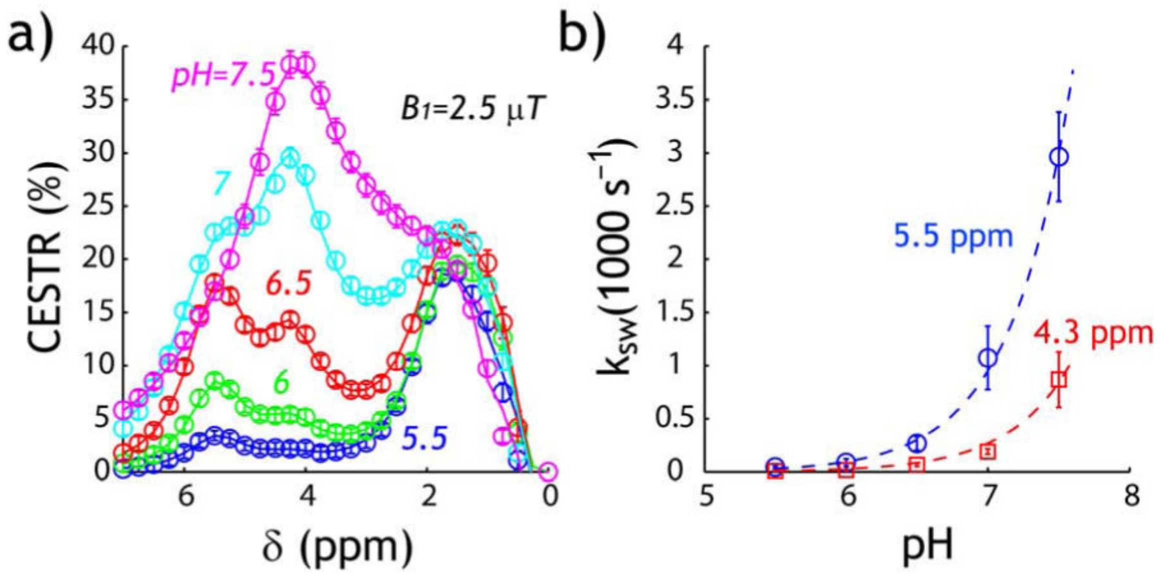

Fig. 5.

Numerical solution of iopamidol pH-dependent chemical exchange properties. a) Numerical fitting of asymmetry plots (B_1 =2.5 μT). b) Numerically determined pH-dependent chemical exchange for labile protons at 4.3 and 5.5 ppm.

Table 1

Numerically determined pH-dependent exchange rates for labile protons at 5.5 (2-hydrooxypropanamido group), 4.3 (amide group), 1.8 (secondary hydroxyl group) and 0.8 (primary hydroxyl groups) ppm. Data are shown in mean ± standard deviation. The relative labile proton ratio for 5.5, 4.3, 1.8 and 0.8 ppm was fixed to be 1:2:1:4, with labile proton ratio at 5.5 ppm determined to be 1:3449 ± 747.

K_{sw} (s^{-1})				
pH	**k_{sw} (5.5 ppm)**	**k_{sw} (4.3 ppm)**	**k_{sw} (1.8 ppm)**	**k_{sw} (0.8 ppm)**
5.5	47 ± 12 s^{-1}	7 ± 4 s^{-1}	388 ± 157 s^{-1}	2070 ± 331 s^{-1}
6	87 ± 34 s^{-1}	17 ± 6 s^{-1}	242 ± 188 s^{-1}	1759 ± 519 s^{-1}
6.5	265 ± 65 s^{-1}	67 ± 15 s^{-1}	416 ± 166 s^{-1}	1856 ± 1567 s^{-1}
7	1074 ± 298 s^{-1}	190 ± 25 s^{-1}	1104 ± 337 s^{-1}	1715 ± 483 s^{-1}
7.5	2896 ± 285 s^{-1}	868 ± 260 s^{-1}	9262 ± 6138 s^{-1}	5117 ± 4485 s^{-1}